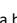

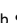



Electronic Supplementary Information (ESI) for

**Interface microenvironment mediates emission of semiconductor
nanocluster via surface-dopant-involved direct charge transfer**

Zhiqiang Wang^{a,b} , Hao Ma^a , Jiayu Zhang^{a,b} , Yingjia Lan^b , Jia-Xing Liu^a, Shang-Fu Yuan^a, Xiao-Ping Zhou^a, Xiaohong Li^b, Chaochao Qin^c, Dong-Sheng Li^d, Tao Wu^{a,b*}

^a College of Chemistry and Materials Science, Guangdong Provincial Key Laboratory of Functional Supramolecular Coordination Materials and Applications, Jinan University, Guangzhou 510632, China.

^b College of Chemistry, Chemical Engineering and Materials Science, Soochow University, Suzhou, Jiangsu 215123, China

^c Henan Key Laboratory of Infrared Materials & Spectrum Measures and Applications, School of Physics, Henan Normal University, Xinxiang 453007, China.

^d College of Materials and Chemical Engineering, Hubei Provincial Collaborative Innovation Centre for New Energy Microgrid, Key Laboratory of Inorganic Nonmetallic Crystalline and Energy Conversion Materials, China Three Gorges University, Yichang 443002, China.

E-mail: wutao@jnu.edu.cn.

Table S1. Results of fitting of Mn^{2+} emission lifetime curves of T4-Mn crystals and d_n dispersions.

Sample	Crystal	d_0	d_1	d_2	d_3	d_4	d_5	d_6
Exponential	Mono	Mono	Double	Double	Mono	Mono	Mono	Mono
A_1	1	1	0.639	0.877	1	1	1	1
τ_1 (μs)	128.0	121.7	14.2	15.8	19.1	24.5	28.5	35.6
A_2	/	/	0.361	0.123	/	/	/	/
τ_2 (μs)	/	/	125.1	120.7	/	/	/	/
τ_{ave} (μs)	128.0	121.7	52.8	28.8	19.1	24.5	28.5	35.6

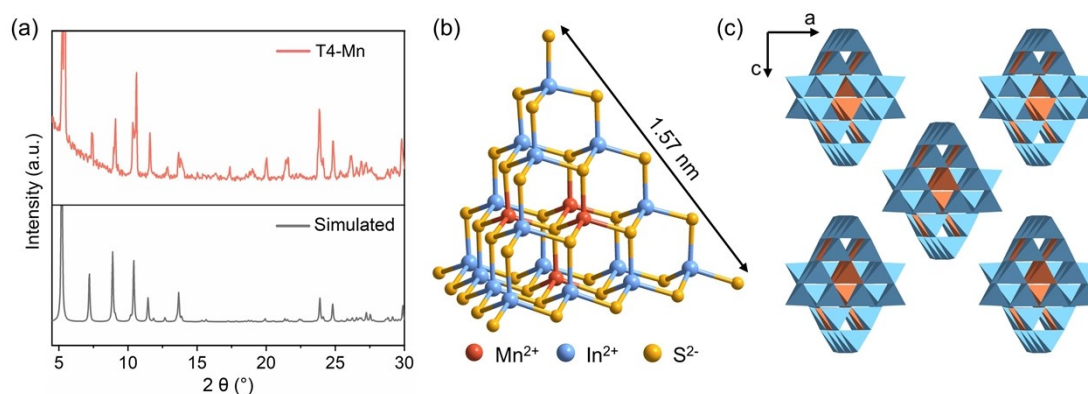


Figure S1. (a) Powder XRD patterns of T4-Mn crystals and the simulated one. (b) Schematic depiction of isolated T4-Mn cluster, which contains 14 negative charges (not shown). (c) Stacking mode of isolated T4-Mn clusters in crystal. Protonated organic amines around T4-Mn clusters are omitted for clarity.

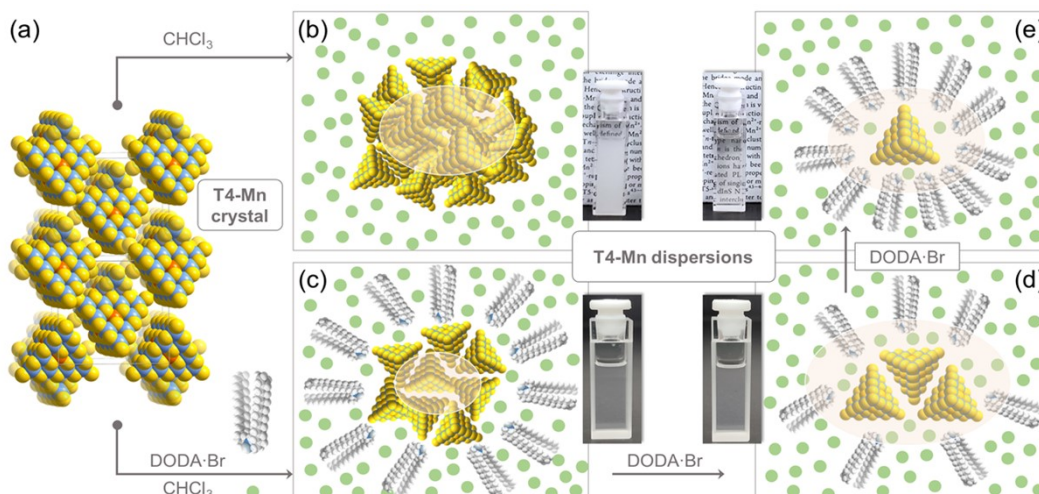


Figure S2. (a) Packing pattern of T4-Mn clusters within crystal (counter cations around clusters are omitted for clarity). Schematics of T4-Mn dispersions and corresponding optical images in chloroform without DODA-Br surfactant (b) and those containing surfactant in increasing amounts (c-e).

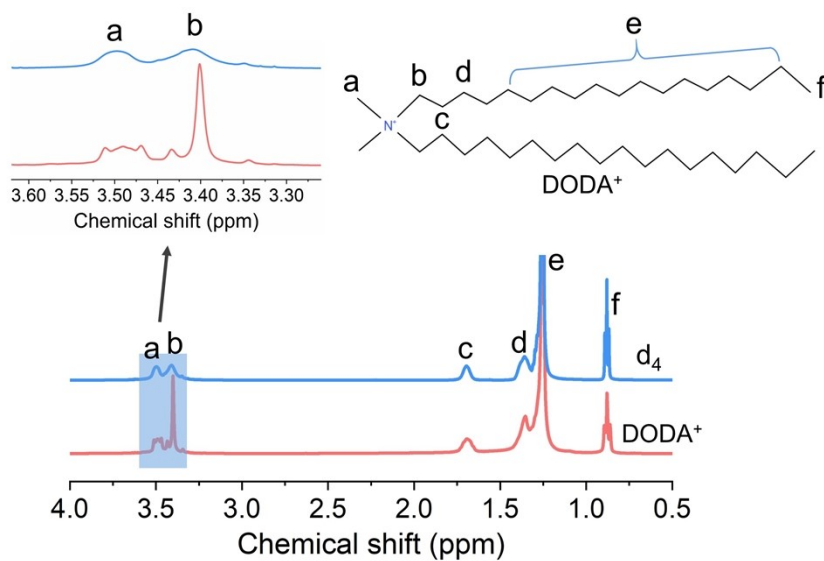


Figure S3. ¹H-NMR spectra of surfactant DODA·Br in chloroform solution and dispersion **d**₄. CDCl₃ and tetramethylsilane were used as solvent and internal standard, respectively. Numbers in figures represent H atom of specific group. Inset on the left shows magnified chemical peaks of H atom from a and b.

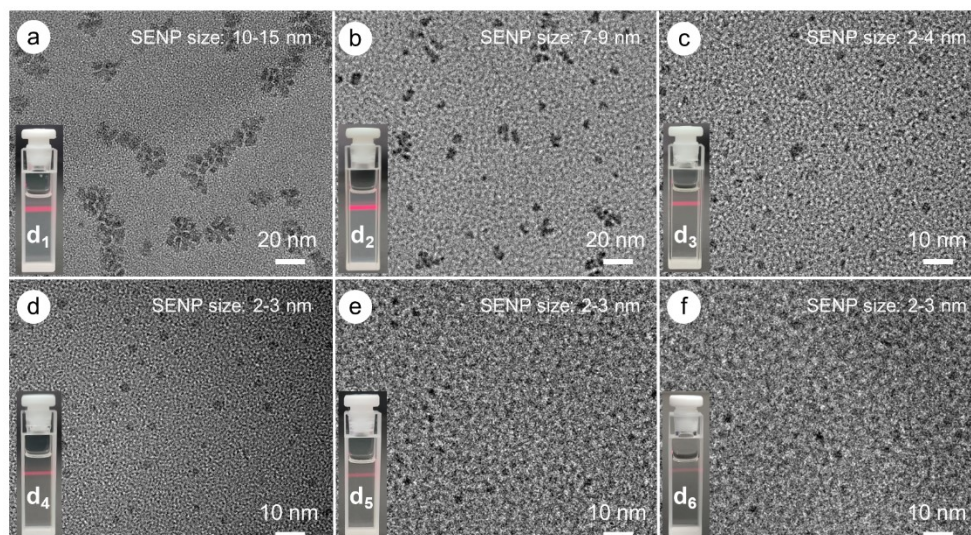


Figure S4. TEM images of SENPs in d_n dispersions ($n = 1-6$). Insets in each sub-graph are optical images showing Tyndall effect of the corresponding dispersion. Obviously, Tyndall effect becomes weaker gradually with increasing addition of DODA-Br, indicating that more DODA-Br leads to better dispersity of T4-Mn clusters.

Surfactant-assisted high dispersity of T4-Mn clusters.

The T4-Mn crystals used were synthesized using a modified solvothermal method.^{1,2} The phase purity of the T4-Mn crystals was confirmed using powder X-ray diffraction analysis (Figure S1a). Specifically, single-crystal X-ray diffraction analysis showed that the T4-Mn crystals were composed of isolated supertetrahedral clusters (Figure S1b) with a uniform size of ~ 1.6 nm (along their edge, these small-sized clusters can be recognized as ultra-small “QDs”), in which four near-surface Mn^{2+} ions were coordinated to a central μ_4-S^{2-} site (i.e., $[Mn_4S]$ core) and symmetrically resided on each face of the supertetrahedron (Scheme 1c). Owing to the strong electrostatic interactions of the clusters (induced by their close packing, Figure S1c) with organic counter cations (i.e., protonated 1,8-diazabicyclo[5.4.0]-undec-7-ene), the T4-Mn crystals did not exhibit good dispersity in common organic solvents. However, the formation of a good dispersion in a solvent is a prerequisite for systematically investigating the EET/ECT processes. Thus, to ensure that the near-surface Mn^{2+} ions within the clusters were maximumly exposed to the IMs in chloroform, a quaternary ammonium surfactant with long alkyl chains, namely, dimethyldioctadecylammonium bromide ($DODA^+Br^-$), was employed as a counter cation and dispersing agent, wherein the $DODA^+$ cations encapsulated the polyanionic

clusters (each cluster contains 14 negative charges) *via* electrostatic interactions and then extracted them into the solvent with the aid of their external long alkyl chains. The successful encapsulation of the clusters by the surfactant molecules was initially confirmed using $^1\text{H-NMR}$ spectroscopy (Figure S3). Specifically, the peaks of chemical shift of the hydrogen atoms in the N-methyl (H_a) and N-methylene (H_b) groups in the cationic head broadened because of the strong electrostatic interactions between the cationic head and polyanionic clusters.³ To optimize the dispersity of the clusters, T4-Mn dispersions (denoted as \mathbf{d}_n , $n = 0-6$) with different surfactant/cluster molar ratios were prepared by dispersing the T4-Mn crystals in chloroform using DODA·Br. Subsequently, the dispersity of the clusters in chloroform was characterized using high-resolution transmission electron microscopy (HR-TEM). As expected, the milky dispersion \mathbf{d}_0 , which did not contain the surfactant, exhibited large-sized particles, which were visible even to the naked eye, suggesting that the clusters were not readily dispersible in pure chloroform (Figure S2b). On the other hand, the clusters dispersed easily in chloroform to form surfactant-encapsulated cluster-based nanoparticles (SENPs) when DODA·Br was used (Figure S2c). The size of the SENPs in these dispersions decreased gradually with an increase in the amount of DODA·Br added, and then plateaued (Figure S2d, e). Compared to dispersion \mathbf{d}_1 , which contained large-sized SENPs (~10–15 nm) (Figure S4a), dispersion \mathbf{d}_2 contained SENPs ~7–9 nm in size (Figure S4b); this is much greater than the size of the individual clusters (~1.6 nm). Therefore, it can be concluded that the clusters were gradually separated from the cluster-assembled SENPs because of DODA·Br. The clusters aggregated to form approximately monodispersed SENPs 2–3 nm in size in the clear dispersions (\mathbf{d}_4 – \mathbf{d}_6) (Figure S4d-f). Due to the mono-exponential decay (Figure 1c) for sample \mathbf{d}_3 – \mathbf{d}_6 , we conjectured that each T4-Mn cluster in the 2-3 nm NPs are being exposed to outer environment. For simplicity, schematic of mono-cluster dispersion was depicted in Scheme 2 and Figure S2 as well as in the text, which would better reveal the coupling interactions of monocluster with interfacial molecules. Owing to the excellent dispersity of the clusters in dispersion \mathbf{d}_4 (similar to that of monocluster) (Figure S4d), it was used for the subsequent experiments to probe the Mn^{2+} -dominated coupling interactions. On the other hand, the change in the size of the SENPs in the dispersions was confirmed to be in keeping with the Tyndall effect (see the insets in Figure S4). In addition, as suggested by our previous report⁴, the sulfur sites in the 6 edges of the clusters are more electron-rich as compared to the sulfur sites in the 4 faces. Therefore, in dispersion \mathbf{d}_4 (each cluster contains 14 negative charges), 14 DODA⁺ would anchor onto the sulfur sites on the edges as a

preference via electrostatic interaction and more space would be left on the 4 faces of cluster for hydrogen bonding with interfacial molecules despite the dynamic equilibrium process.

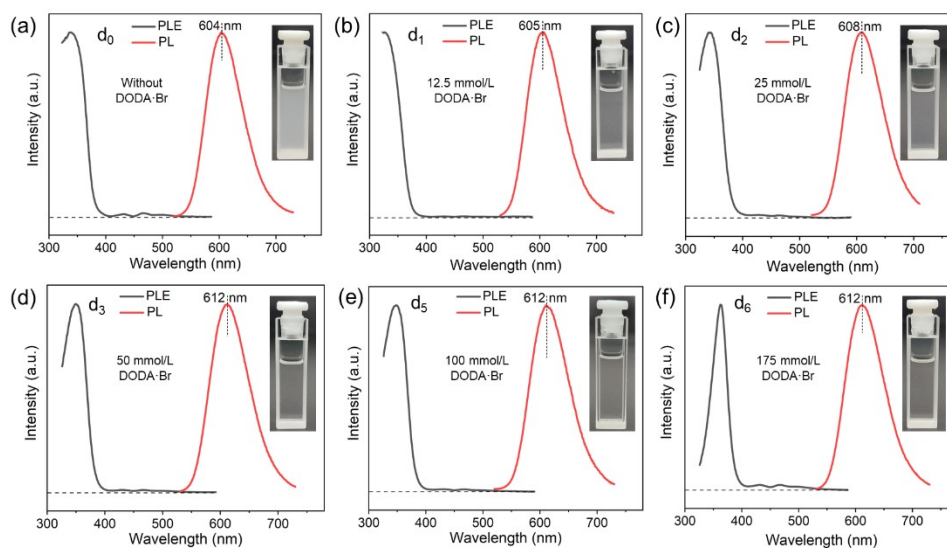


Figure S5. PLE and PL spectra of dispersions with chloroform as solvent: (a) d_0 , (b) d_1 , (c) d_2 , (d) d_3 , (e) d_5 , and (f) d_6 . Except dispersion d_0 , dispersions d_{1-6} were used after centrifugation.

When a few amounts of DODA·Br was added in chloroform solvent, T4-Mn crystals usually dispersed into relatively large-sized SENPs, and solvent molecules only interact with clusters locating at outside of big SENPs, instead of ones inside of SENPs. When more DODA·Br surfactant was added, SENPs continue dispersing into solvent, leading to the formation of small SENPs with sizes of 2–3 nm. For these SENPs, surface of clusters maximumly collide and interact with solvent molecules. When the amount of DODA·Br was continuously increased, dispersed cluster may be encapsulated by more DODA⁺ ions via electrostatic interactions. Thus for, the number of solvent molecules that collide and interact with clusters were reduced due to steric hinderance. Additionally, the superfluous DODA·Br in chloroform would enhance the viscosity of dispersion, which to some extent restrict the movability of solvent molecules and relax the collision between clusters and chloroform molecules. Mn²⁺ emission of dispersion d_0 peaks at 604 nm, which is the same as that of T4-Mn crystals, indicating the negligible effect from surrounding molecules. With DODA·Br added, the milky status of dispersions gradually disappeared, implying the improved dispersity of clusters in chloroform. Additionally, compared with T4-Mn crystals, d_{1-6} dispersions displayed red-shifted Mn²⁺ emission. With increasing amount of DODA·Br, an increased red-shift of Mn²⁺ emission was initially observed, and then the

emission peak was unchanged at 612 nm even with increasing amount of DODA·Br. All dispersions exhibited weak excitation band (400–550 nm) for directly exciting Mn^{2+} ions.

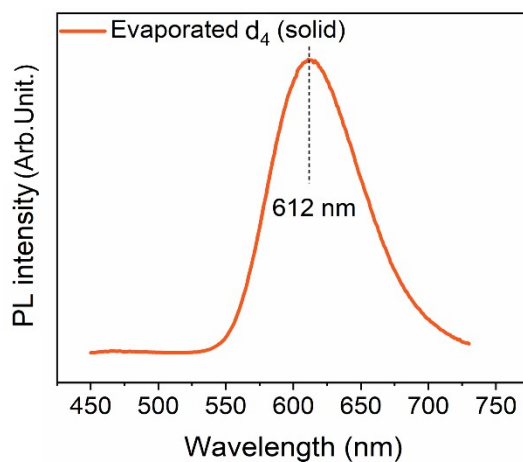


Figure S6 PL spectrum ($\lambda_{\text{ex}} = 356$ nm) of the solid-state sample obtained from dispersion d_4 via dry treatment (i.e., chloroform solvent was evaporated). Mn^{2+} emission of this sample still peaks at 612 nm, indicating that chloroform molecules impose no effect on PL wavelength of Mn^{2+} emission. Compare to T4-Mn crystals, the redshift of Mn^{2+} emission is attributed to DODA⁺ cations close to clusters.

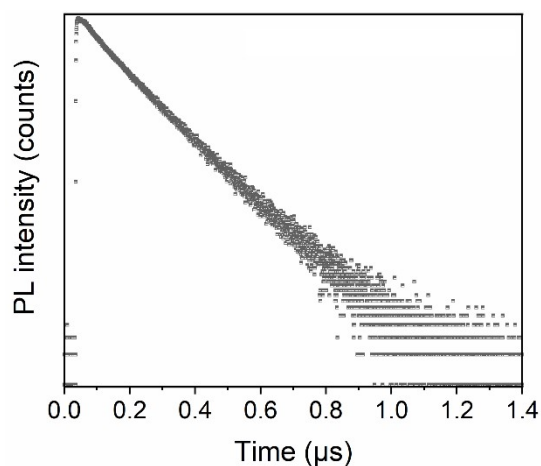


Figure S7. PL decay curve of dispersion d_0 .

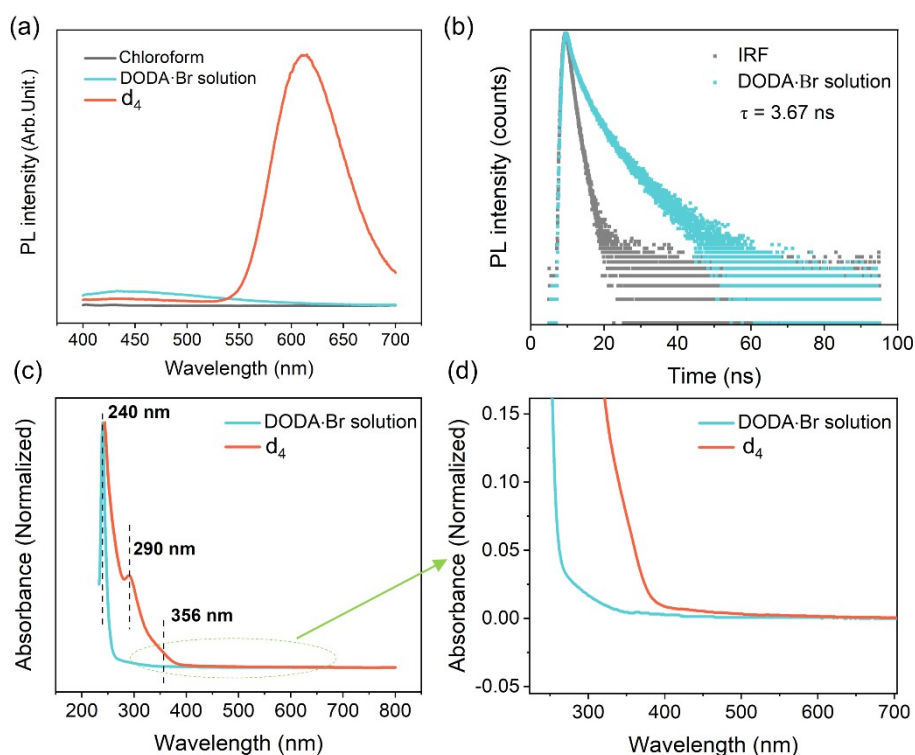


Figure S8. (a) PL spectra of chloroform, chloroform with DODA·Br dissolved (75 mmol/L), dispersion d_4 . Chloroform shows no PL emission. DODA·Br in chloroform presents weak emission in comparison with d_4 dispersion. (b) PL decay curve of DODA·Br in chloroform ($\lambda_{\text{ex}} = 356$ nm and $\lambda_{\text{em}} = 612$ nm). TCSPC apparatus instrument response function (IRF) is also given in gray. Nanosecond-level decay lifetime of DODA·Br suggests that surfactant molecules have negligible impact on detecting decay lifetime of Mn^{2+} emission. (c) UV-Vis absorption spectra of dispersion d_4 and DODA·Br in chloroform. No absorption was detected at 356 nm from DODA·Br solution. (d) Enlarged absorption spectra from Figure S8c. Weak absorption from 400 nm to 550 nm was also observed for dispersion d_4 .

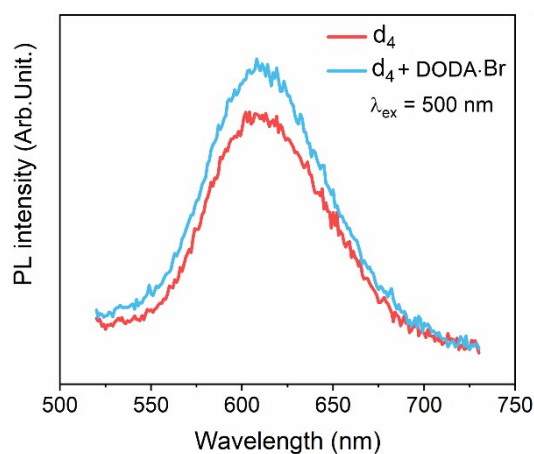


Figure S9. PL spectra of dispersion d_4 ($\lambda_{\text{ex}} = 500$ nm) with and without extra addition of DODA·Br (25

mmol/L).

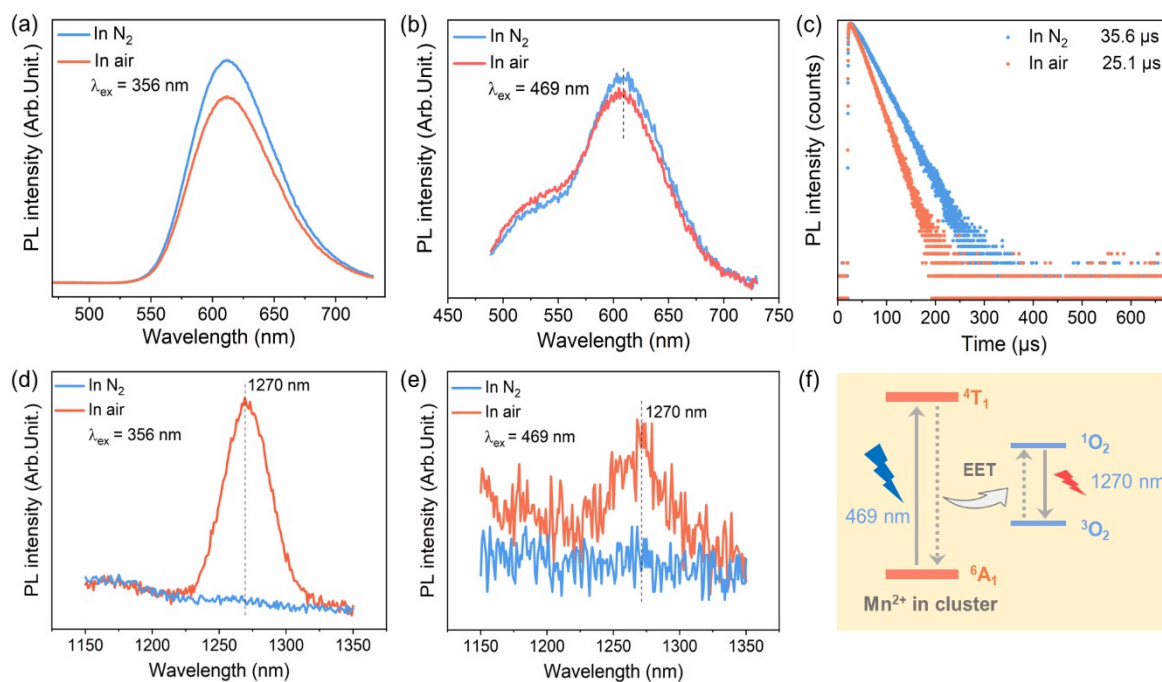


Figure S10. (a) and (b) PL spectra of clusters in dispersion **d₄** in N₂ atmosphere and ambient air under excitation at 356 and 469 nm, respectively. (c) Decay curves ($\lambda_{\text{em}} = 612$ nm and $\lambda_{\text{ex}} = 356$ nm) of the Mn²⁺ emission from dispersion **d₄** in N₂ atmosphere and air. (d) and (e) Near-infrared PL spectra of ¹O₂ molecules in dispersion **d₄** in N₂ atmosphere and ambient air under excitation at 356 and 469 nm, respectively. (f) Schematic illustration of EET from directly excited Mn²⁺ ions to ³O₂ molecules, resulting in ¹O₂ emission.

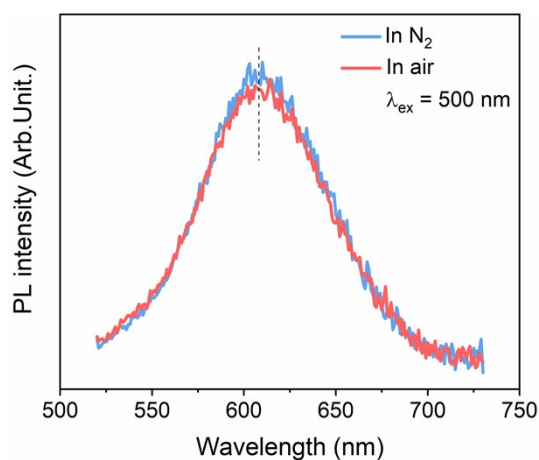


Figure S11. PL spectra of dispersion **d₄** in N₂ atmosphere and ambient condition ($\lambda_{\text{ex}} = 500$ nm).

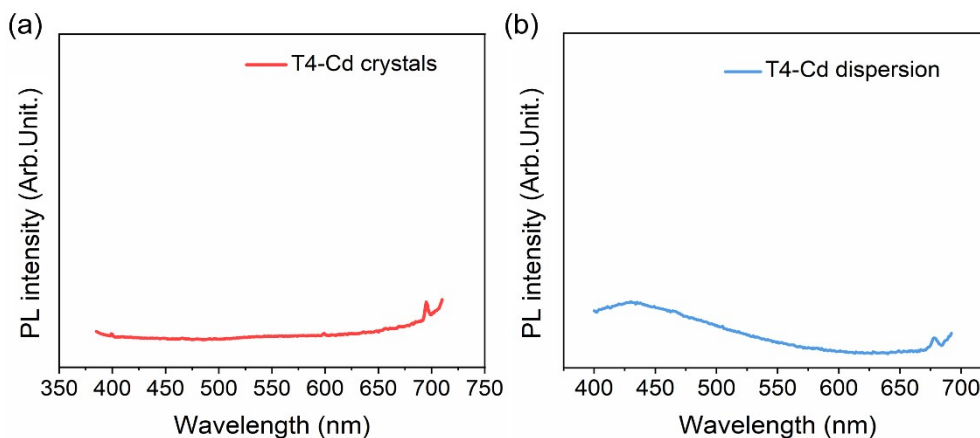


Figure S12. (a) PL spectrum of T4-Cd crystals. (b) PL spectrum of T4-Cd dispersion, which was prepared according to the same dispersing condition with that of T4-Mn dispersion (\mathbf{d}_4). No PL emission in the visible light region was detected from T4-Cd crystals, and weak emission centered at ~ 430 nm from T4-Cd dispersion was observed, which may be attributed to emission from DODA-Br.

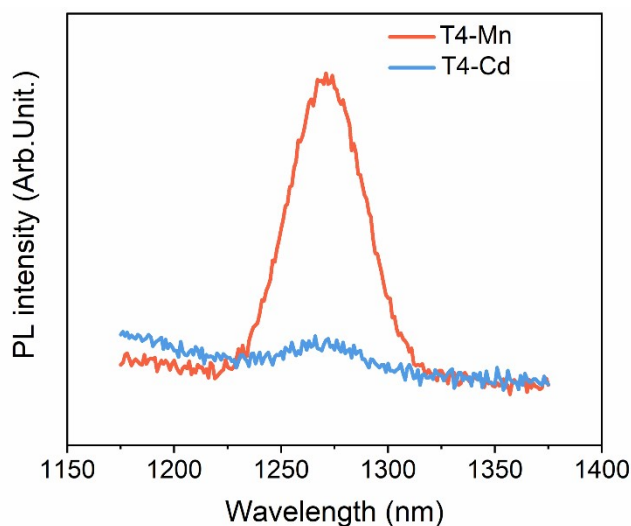


Figure S13. (a) Room-temperature near-infrared PL spectra of $^1\text{O}_2$ from \mathbf{d}_4 and T4-Cd dispersions in ambient condition under 356 nm excitation. $^1\text{O}_2$ emission peaked at 1270 nm from \mathbf{d}_4 is much stronger in intensity than that from T4-Cd dispersion, revealing that Mn^{2+} ions in cluster play significant role in generating $^1\text{O}_2$.

Effects of interfacial $^3\text{O}_2$ molecules on Mn^{2+} emission.

The Mn^{2+} emission intensity of dispersion \mathbf{d}_4 in response to excitation at 356 nm in air was found to be slightly lower than that in a N_2 atmosphere (Figure S10a). Moreover, this dispersion also exhibited a characteristic near-infrared emission centered at 1270 nm, which was related to singlet oxygen ($^1\text{O}_2$),

in ambient atmosphere⁵ but not in a N₂ atmosphere (Figure S10d). These results suggested that the decrease in the Mn²⁺ emission intensity was correlated to EET from the excited-state clusters to the ³O₂ molecules.

Given that the PL decay dynamics can provide fundamental insights into the EET process⁶, time-resolved emission decay measurements were performed on dispersion **d₄** both without ³O₂ and in its presence (Figure S10c). The Mn²⁺ emission decay lifetime of the dispersion ($\lambda_{\text{ex}} = 365$ nm) in ambient air (25.1 μs) was slightly smaller than that in a N₂ atmosphere (35.6 μs). This was because of the consumption of the excited-state energy by the interfacial ³O₂ molecules. To investigate the possibility of direct coupling between the Mn²⁺ ions and ³O₂ molecules, the Mn²⁺ emission in response to the direct excitation on the Mn²⁺ ions was measured. The Mn²⁺ emission intensity of **d₄** upon excitation at 469nm (Figure S10b) and 500 nm (Figure S11) in air was found to be slightly lower compared with that in a N₂ atmosphere. In addition, a relatively weak ¹O₂ emission was detected after the direct excitation of the Mn²⁺ ions (Figure S10e). In contrast to previous reports on the O₂-involved modulation of the Mn²⁺ emission^{7,8}, this is the first case that exhibits the direct EET from excited-state Mn²⁺ to ³O₂ molecules. For example, Chen et al. reported that O₂ molecules can disturb the ligand field of the near-surface Mn²⁺ ions in doped perovskite nanocrystals and thus affect the Mn²⁺ emission, including its intensity and decay dynamics⁷. In addition, Li and coworkers reported that the ¹O₂ emission from Mn²⁺-doped perovskite nanocrystals is related to the surface Mn²⁺ defect states⁸. Note that, in the case of Mn²⁺-doped CsPbCl₃ nanocrystals in an O₂ environment, the decay profile of the Mn²⁺ emission changed from one based on a single exponential to one based on two exponentials. However, that of the Mn²⁺ emission of dispersion **d₄** in air remained one based on a single exponential. Owing to the unique structure of the clusters, in which each Mn²⁺ ion has the same probability of coupling with the ³O₂ molecules, and given that the time scale (ns or ps) for EET from Mn²⁺ to O₂ is much shorter than that of the Mn²⁺ emission (μs), the unaltered single-exponential decay profile was to be expected. In addition, the decay lifetime of the Mn²⁺ emission of dispersion **d₄** in a N₂ atmosphere was much shorter than that of the emission of the T4-Mn crystals in air, suggesting that the shortened decay lifetime in the case of the clusters in dispersions was mainly caused by the chloroform molecules. We used isostructural T4-Cd clusters without any near-surface Mn²⁺ ions for comparison. No obvious ¹O₂ emission was observed, thus further highlighting the significance of the Mn²⁺ ions with respect to the direct EET process (Figure S12 and S13).

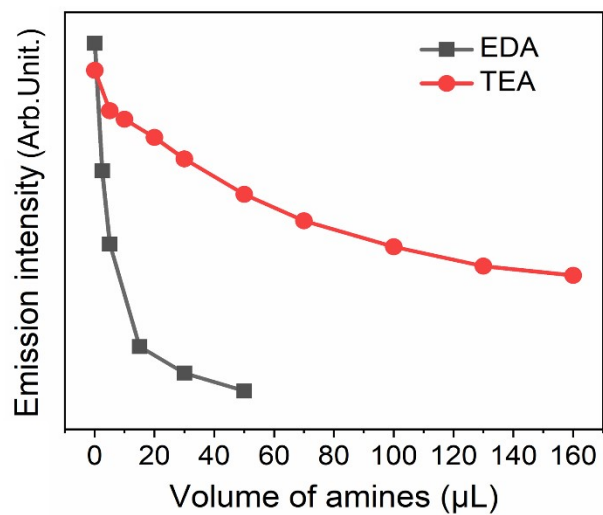


Figure S14. Plot of emission intensity of dispersion d_4 as a function of amounts of EDA (or TEA).

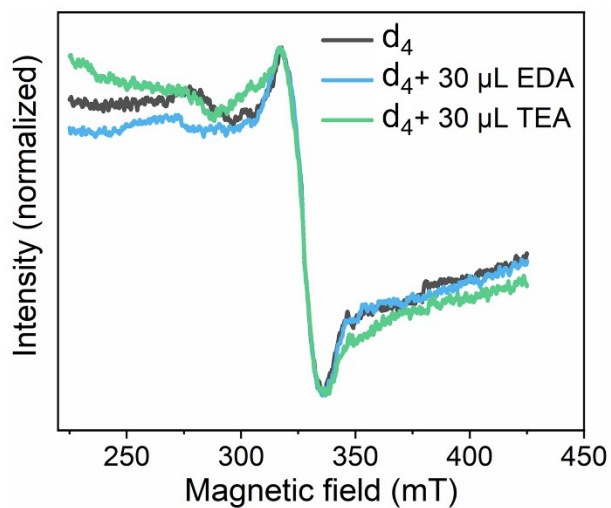


Figure S15. EPR spectra of dispersion d_4 samples with and without EDA (or TEA).

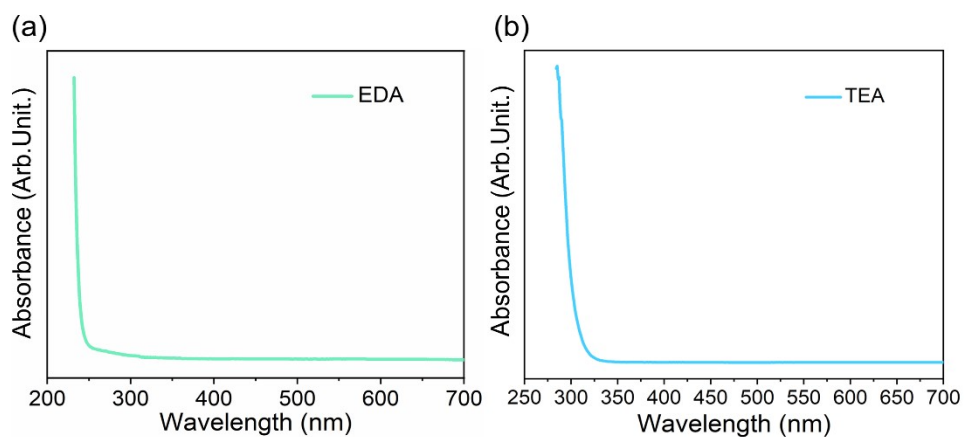


Figure S16. UV-Vis absorption spectra of (a) EDA and (b) TEA. No absorption was found in the range of 350–500 nm, which means that only clusters, instead of amine molecules, can be excited under excitation at 350–500 nm.

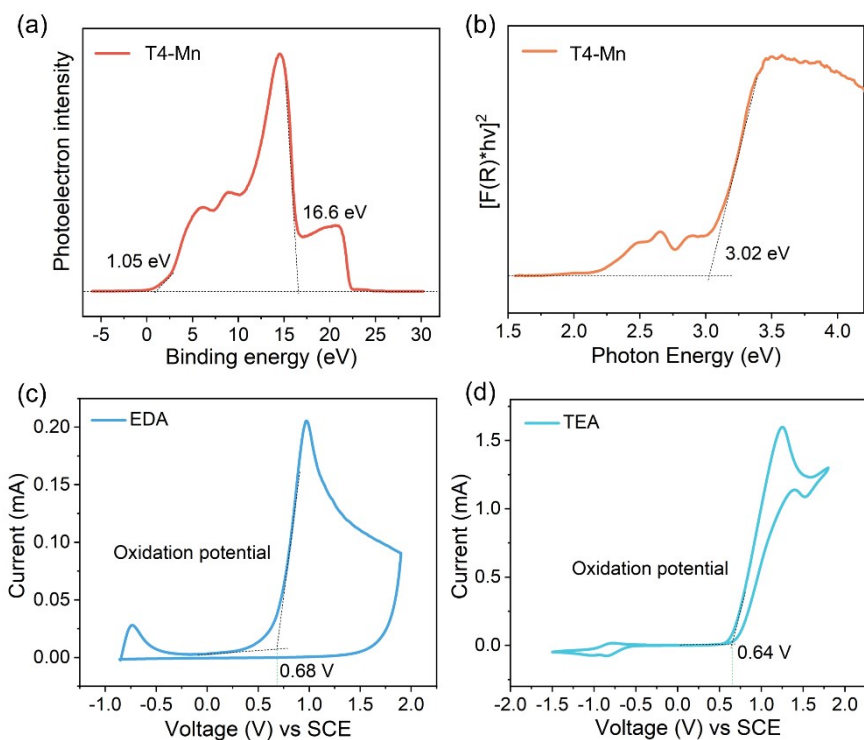


Figure S17. (a) UPS data for T4-Mn crystals. (b) Tauc plot of T4-Mn crystals based on UV-Vis diffusive reflectance spectra obtained at room temperature. The energy level of T4-Mn cluster can be calculated as: $E_{VB} = (16.6 - 21.22) \text{ eV} - 1.05 \text{ eV} = -5.67 \text{ eV}$, $E_{CB} = -5.67 \text{ eV} + 3.02 \text{ eV} = -2.65 \text{ eV}$. (c) and (d) CV curves of EDA and TEA, respectively.

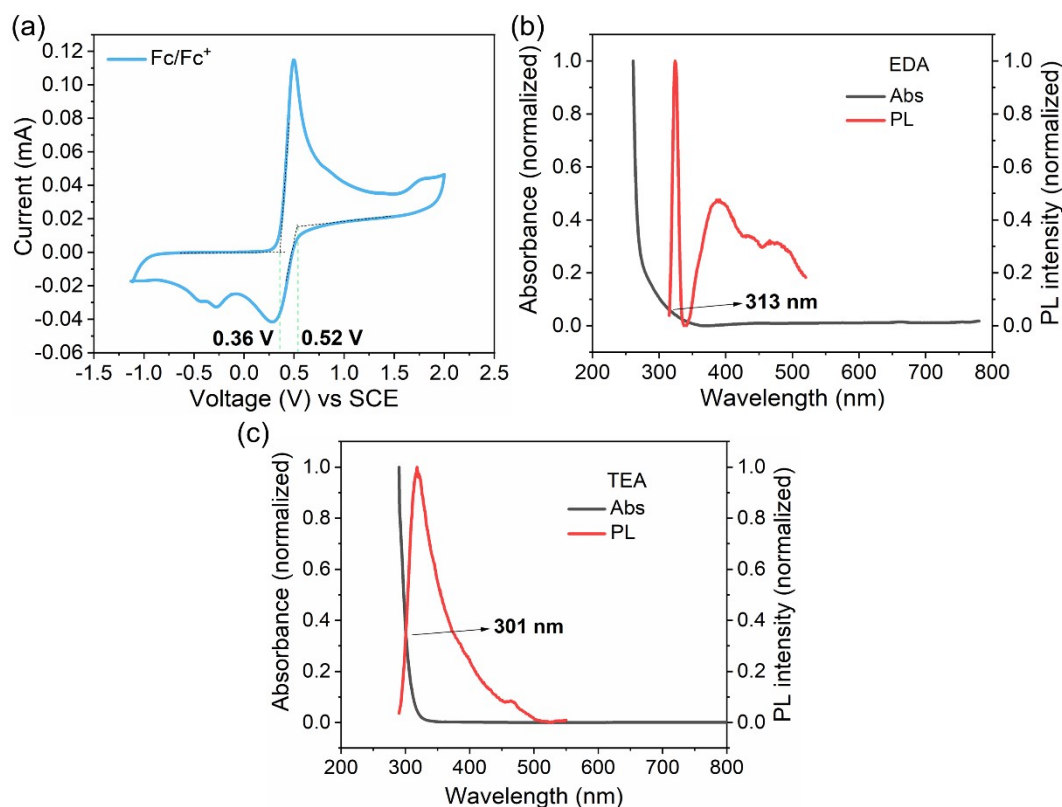


Figure S18. (a) CV curve of Fc/Fc⁺ (calibration standard). Normalized UV-Vis absorption and PL spectra of (b) EDA and (c) TEA.

Energy levels determination for EDA. According to cyclic voltammogram of ferrocene, $E(\text{Fc}/\text{Fc}^+)$ is 0.44 V (vs SCE). According to Figure S17c, the oxidation potential of EDA (E^{ox}) was determined to be 0.68 V. The potential of Fc/Fc⁺ vs vacuum is 4.8 V. The energy level of HOMO of EDA can be calculated as: $E_{\text{HOMO}} = -[E^{\text{ox}} - E(\text{Fc}/\text{Fc}^+) + 4.8]$ eV = $-[(0.68 - (0.36 + 0.52)/2) + 4.8]$ eV = -5.04 eV. The reduction potential of EDA was not obtained from CV data, therefore it was estimated using: $E_{\text{LUMO}} = E_{\text{HOMO}} + E_g$, in which E_g is optical gap of EDA molecule. E_g of EDA was determined from the point of intersection between normalized absorption and PL emission spectra in Figure S18b. Thus, E_{LUMO} of EDA was calculated as: $E_{\text{LUMO}} = E_{\text{HOMO}} + E_g = -5.04 + 3.96 = -1.08$ eV^{9,10}.

Energy levels determination for TEA. According to Figure S17d, the oxidation potential of TEA (E^{ox}) was determined to be 0.64 V. The potential of Fc/Fc⁺ vs vacuum is 4.8 V. The energy level of HOMO of TEA can be calculated as: $E_{\text{HOMO}} = -[E^{\text{ox}} - E(\text{Fc}/\text{Fc}^+) + 4.8]$ eV = $-[(0.64 - (0.36 + 0.52)/2) + 4.8]$ eV = -5.0 eV. E_g of TEA was determined from the point of intersection between normalized absorption and PL emission spectra in Figure S 18c. E_{LUMO} of TEA can be calculated as: $E_{\text{LUMO}} = E_{\text{HOMO}} + E_g = -5.0 + 4.12 =$

-0.88 eV.

Alignment of energy levels of T4-Mn clusters and amine molecules.

Considering that the Mn^{2+} emission characteristics are directly influenced by the IMs, we assumed that there is direct EET or ECT between the Mn^{2+} ions and IMs. As there was no overlap between the Mn^{2+} emission spectrum and the absorption spectra of the amines, Förster resonance EET was ruled out (Figure S16)¹¹. Therefore, we concluded that the ECT process, which affects the Mn^{2+} emission, was the key. Given the electron-rich nature of neutral organic amines¹², it was assumed that the electrons in the primary amine are transferred to the T4-Mn clusters, resulting in the quenching of the Mn^{2+} emission. To confirm this, the energy levels of the T4-Mn clusters and the organic amines used were estimated based on the results of ultraviolet photoelectron spectroscopy (UPS), UV-Vis absorption spectroscopy, and cyclic voltammetry (CV). Based on the UPS and UV-Vis data (Figure S17a, b), the minimum conduction band (CB) and maximum valence band (VB) levels of the T4-Mn clusters were determined to be -2.65 and -5.67 eV, respectively^{13,14}. According to previous reports, the ${}^4\text{T}_1 \rightarrow {}^6\text{A}_1$ transition levels of Mn^{2+} ions generally reside within the CB and VB levels of the host^{15,16}. In addition, the LUMO and HOMO energy levels of EDA and TEA were calculated based on the CV results and UV-Vis absorption and PL spectra (Figure S17c, d, and S18). The energy levels of the clusters and amines (EDA and TEA) are shown in Figure S17e. It can be seen that electron transfer from the CB of the cluster (or ${}^4\text{T}_1$ level of the Mn^{2+} ions) to the LUMO of the amines is energetically unfavorable; however, hole transfer from the VB of the clusters to the HOMO of the amines is favorable. In other words, electron transfer from the HOMO of the amines to the VB of the clusters is allowed. Furthermore, because of the direct coupling interactions between the Mn^{2+} ions and amines, it is rational that the ${}^6\text{A}_1$ level of the Mn^{2+} ions is thought to be lower than the HOMO level of the amines. As a result, hole transfer from the ${}^6\text{A}_1$ level of the Mn^{2+} ions to the HOMO level of amines is favored (Figure S 17e). Therefore, when the host clusters are excited, fast host-to- Mn^{2+} IET occurs first and is followed by ECT between the Mn^{2+} ions and amines. Moreover, when the Mn^{2+} ions in the cluster, instead of the host clusters, were excited directly, direct ECT occurred between the Mn^{2+} ions and amines.

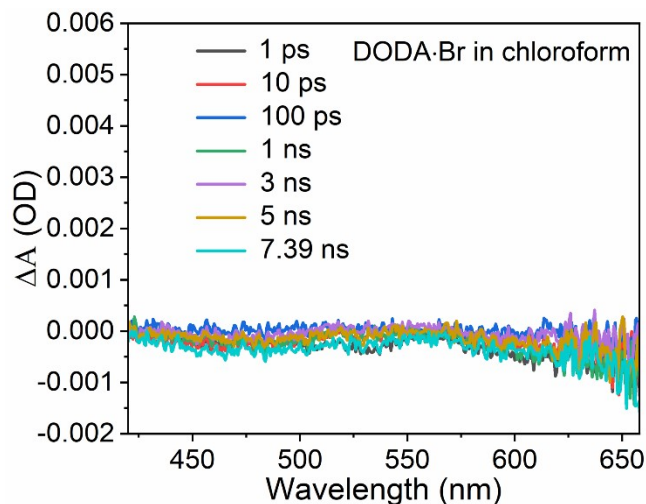


Figure S19. TA spectra of DODA·Br in chloroform excited by 365 nm pulses (the content of DODA·Br is similar with that in pristine dispersion \mathbf{d}_4). No TA signals were detected from DODA·Br solution.

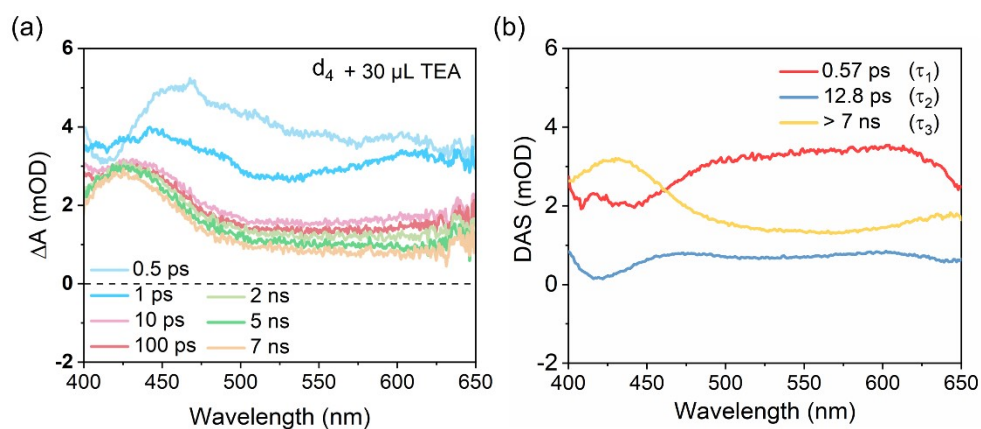


Figure S20. (a) fs-TA spectra of dispersion \mathbf{d}_4 with 30 μL of TEA at several representative time delays ($\lambda_{\text{ex}} = 365 \text{ nm}$). (b) Related decay associated spectra (DAS). TA spectra of dispersion \mathbf{d}_4 with TEA is similar to that of pristine dispersion \mathbf{d}_4 in different time delays. Global analysis gives three kinetic components: 0.57 ps (τ_1), 12.8 ps (τ_2), and $>7 \text{ ns}$ (τ_3). Given that the component constants are similar to that of pristine dispersion \mathbf{d}_4 , we conjectured that ECT between Mn^{2+} in cluster and TEA should be included in the component of $>7 \text{ ns}$ (τ_3).

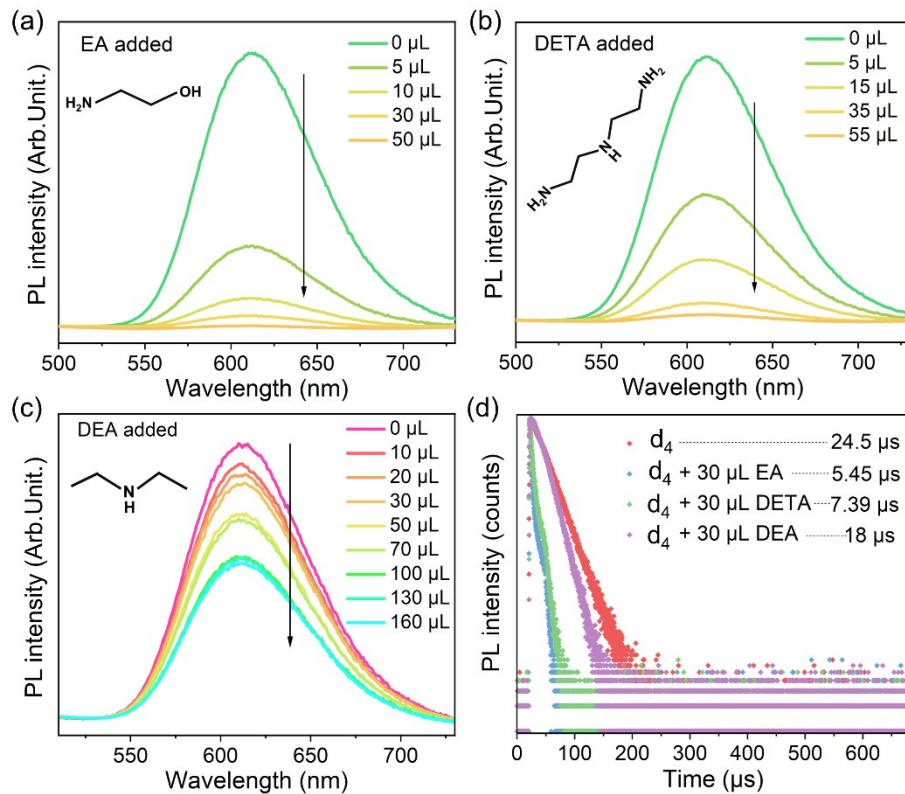


Figure S21. (a-c) PL spectra of dispersions d_4 (3 mL) with raising the addition amount of EA, DETA, and DEA, respectively. (d) PL decay curves of dispersion d_4 samples before and after addition of 30 μL EA, DETA, and DEA ($\lambda_{\text{ex}} = 356 \text{ nm}$ and $\lambda_{\text{em}} = 612 \text{ nm}$).

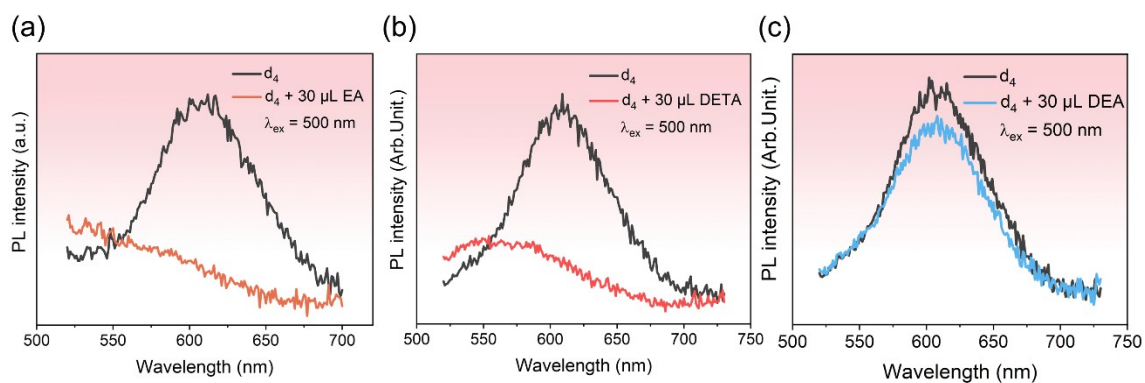


Figure S22. PL spectra of dispersion d_4 samples ($\lambda_{\text{ex}} = 500 \text{ nm}$) with and without 30 μL (a) EA, (b) DETA, and (c) DEA.

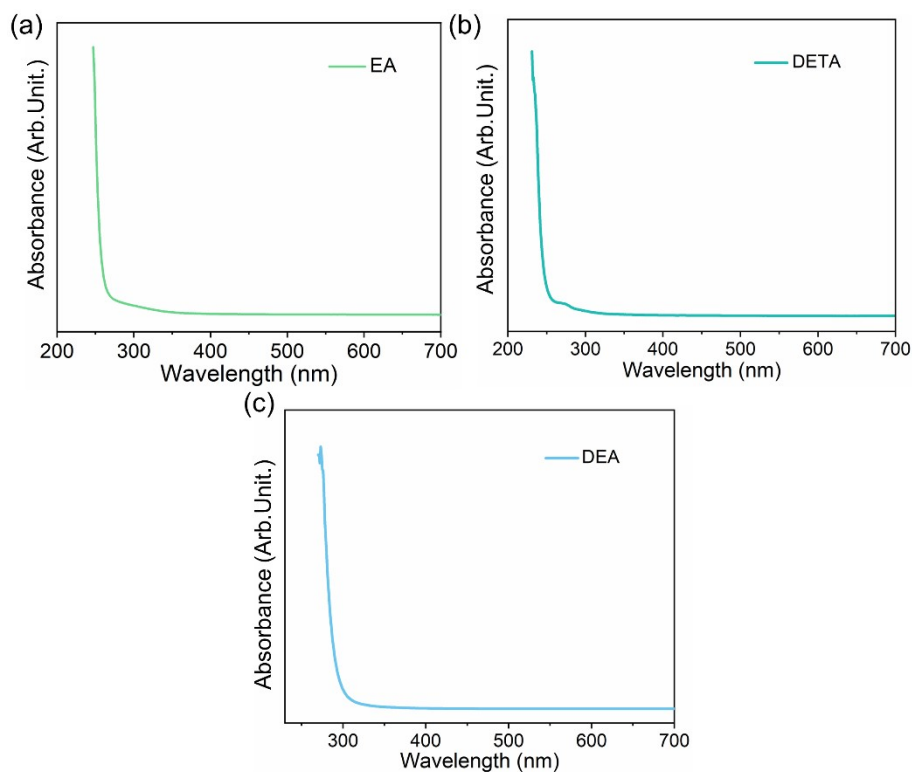


Figure S23. UV-Vis absorption spectra of (a) EA, (b) DETA, and (c) DEA. These results exclude the possibility of Förster resonance energy transfer between excited-state Mn^{2+} ions and amine molecules above.

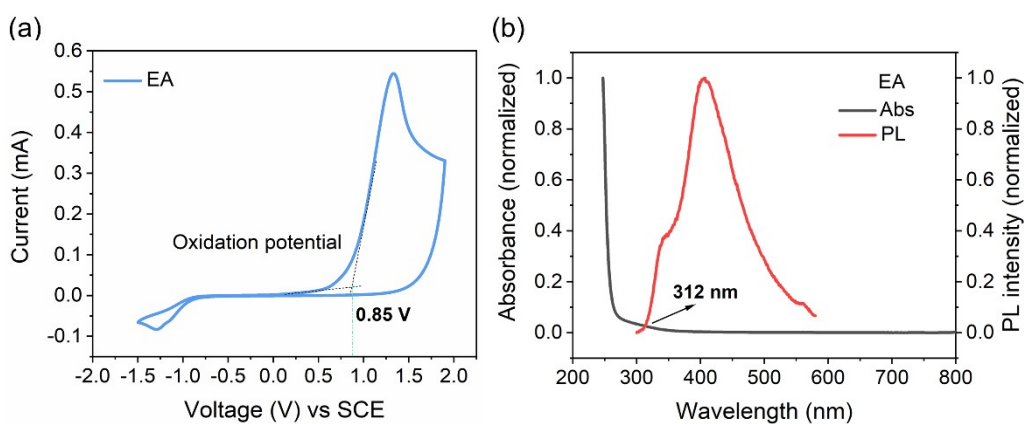


Figure S24. (a) CV curve of EA. (b) Normalized UV-Vis absorption and PL spectra of EA.

Energy levels determination for EA. According to (a), the oxidation potential of EA (E^{ox}) was determined to be 0.85 V. The potential of Fc/Fc^+ vs vacuum is 4.8 V. The energy level of HOMO of EA can be calculated as: $E_{\text{HOMO}} = -[E^{\text{ox}} - E(\text{Fc}/\text{Fc}^+) + 4.8] \text{ eV} = -[(0.85 - (0.36 + 0.52))/2 + 4.8] \text{ eV} = -5.21 \text{ eV}$. E_g of EA can be determined from the point of intersection between normalized absorption and PL

spectrum in (b). E_{LUMO} of EA was calculated as: $E_{\text{LUMO}} = E_{\text{HOMO}} + E_{\text{g}} = -5.21 + 3.97 = -1.24$ eV.

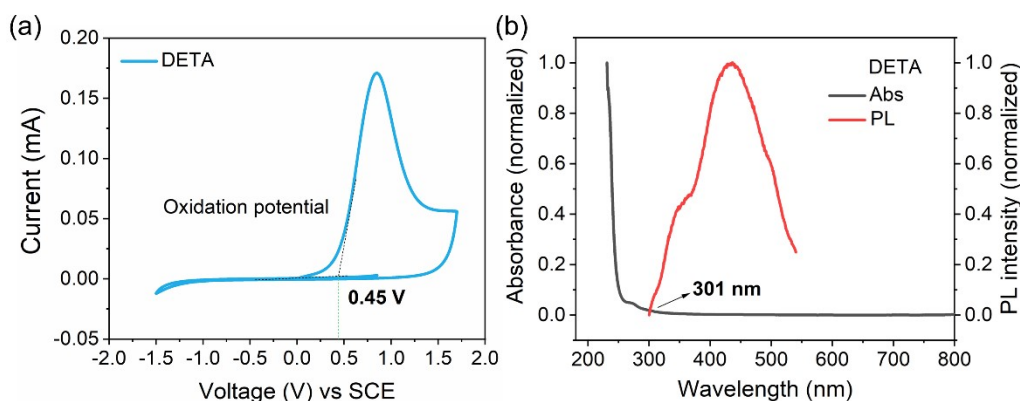


Figure S25. (a) CV curve of DETA. (b) Normalized UV-Vis absorption and PL spectra of DETA.

Energy levels determination for DETA. According to (a), the oxidation potential of FA (E^{ox}) was determined to be 0.45 V. The potential of Fc/Fc^+ vs vacuum is 4.8 V. The energy level of HOMO of DETA can be calculated as: $E_{\text{HOMO}} = -[E^{\text{ox}} - E(\text{Fc}/\text{Fc}^+) + 4.8]$ eV = $-[(0.45 - (0.36 + 0.52)/2) + 4.8]$ eV = -4.81 eV. E_{g} of DETA can be determined from the point of intersection between normalized absorption and PL spectrum in (b). E_{LUMO} of DETA was calculated as: $E_{\text{LUMO}} = E_{\text{HOMO}} + E_{\text{g}} = -4.81 + 4.12 = -0.69$ eV.

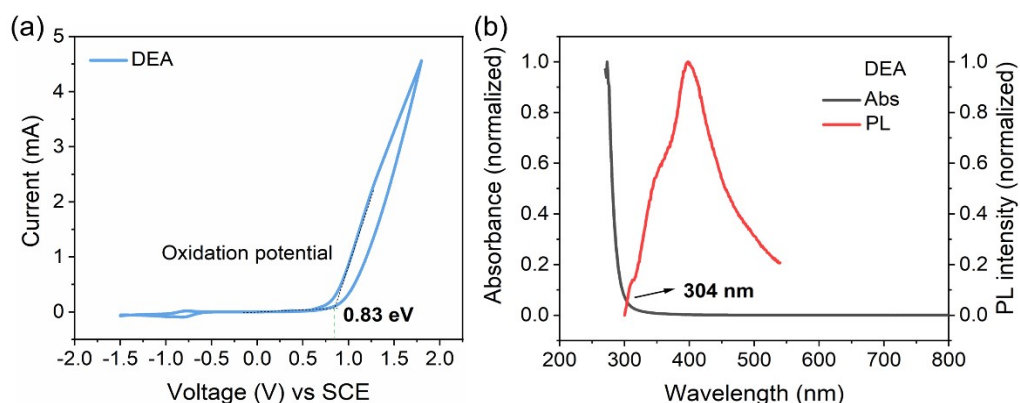


Figure S26. (a) CV curve of DEA. (b) Normalized UV-Vis absorption and PL spectra of DEA.

Energy levels determination for DEA. According to (a), the oxidation potential of DEA (E^{ox}) was determined to be 0.83 V. The potential of Fc/Fc^+ vs vacuum is 4.8 V. The energy level of HOMO of DEA can be calculated as: $E_{\text{HOMO}} = -[E^{\text{ox}} - E(\text{Fc}/\text{Fc}^+) + 4.8]$ eV = $-[(0.83 - (0.36 + 0.52)/2) + 4.8]$ eV = -5.19 eV. E_{g} of DEA can be determined from the point of intersection between normalized absorption and PL spectrum in (b). E_{LUMO} of DEA was calculated as: $E_{\text{LUMO}} = E_{\text{HOMO}} + E_{\text{g}} = -5.19 + 4.08 = -1.11$ eV.

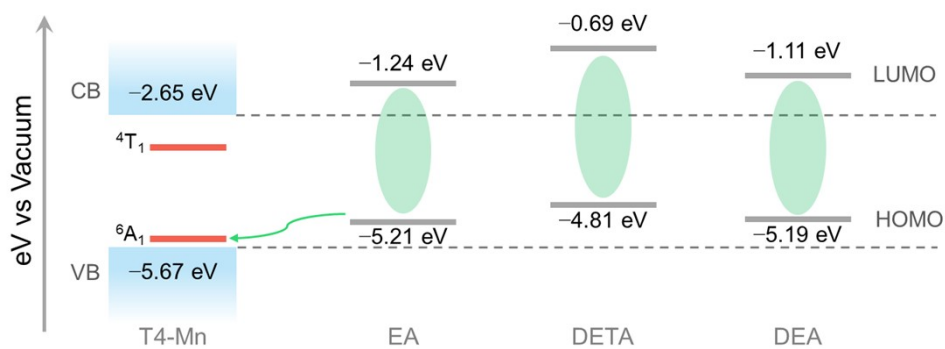


Figure S27. (a) Qualitative energy level alignment of T4-Mn cluster, EA, DETA, and DEA determined from UPS and CV as well as UV-Vis absorption measurements, showing the favored electron transfer from HOMO of amines to 6A_1 state of Mn^{2+} ion.

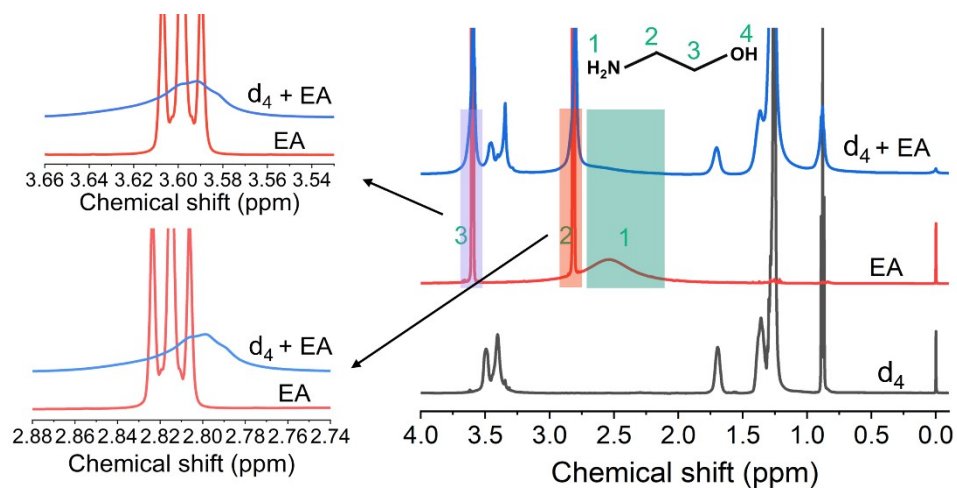


Figure S28. 1H -NMR spectra for d_4 , EA, and their mixture using $CDCl_3$ as solvent. The peak at 2.54 ppm (**1**) for EA is missing for dispersion d_4 with the addition of EA molecules, suggesting the generation of hydrogen bonds between clusters and EA molecules. The peak splitting in **2** and **3** for $-CH_2-$ groups from EA disappeared, and a broad signal was observed for the mixture.

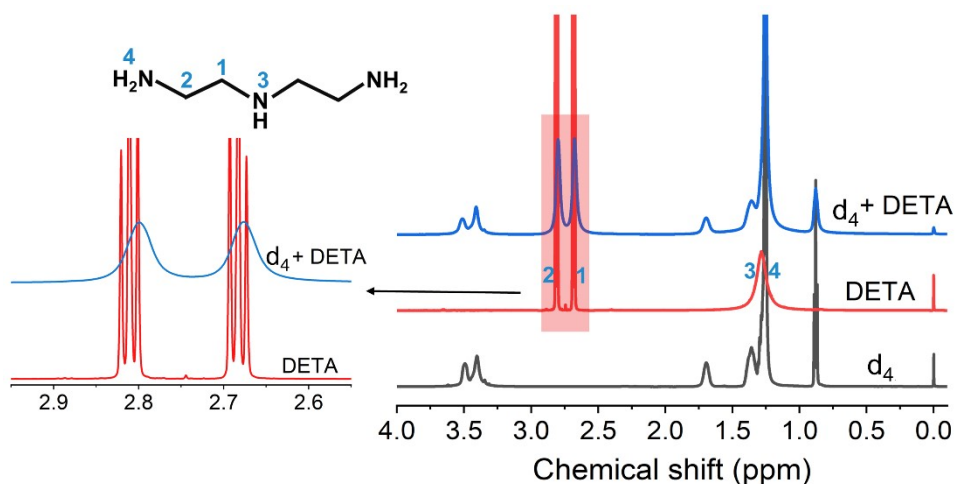


Figure S29. $^1\text{H-NMR}$ spectra for d_4 , DETA, and their mixture using CDCl_3 as solvent. The splitting peaks of $-\text{CH}_2$ groups are converted to broad signals, revealing the generation of hydrogen bonding between clusters and DETA molecules.

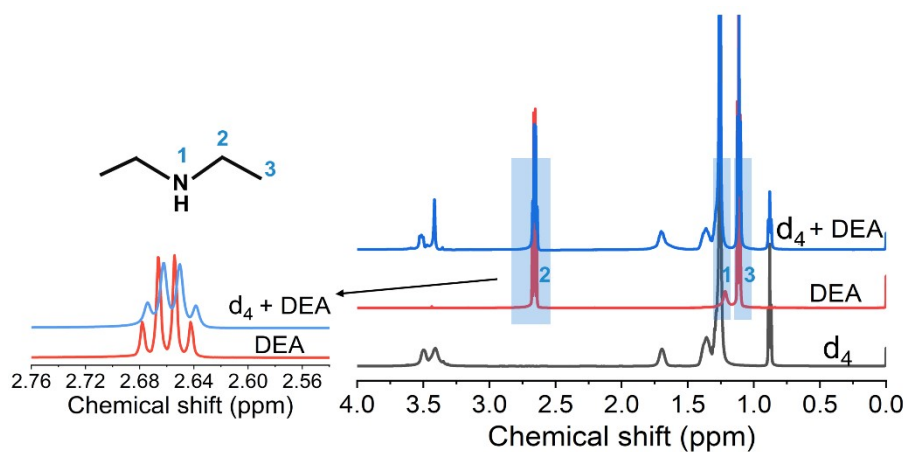


Figure S30. $^1\text{H-NMR}$ spectra for d_4 , DEA, and their mixture using CDCl_3 as solvent. Similar to TEA, no obvious alteration was observed for chemical shift of $-\text{CH}_2$ groups and the coupling splitting, indicating no effective hydrogen bonding between DEA and clusters. Chemical shift peak at 1.21 ppm (1) of DEA should be included in the strong peak at 1.25 ppm for DODA-Br surfactant.

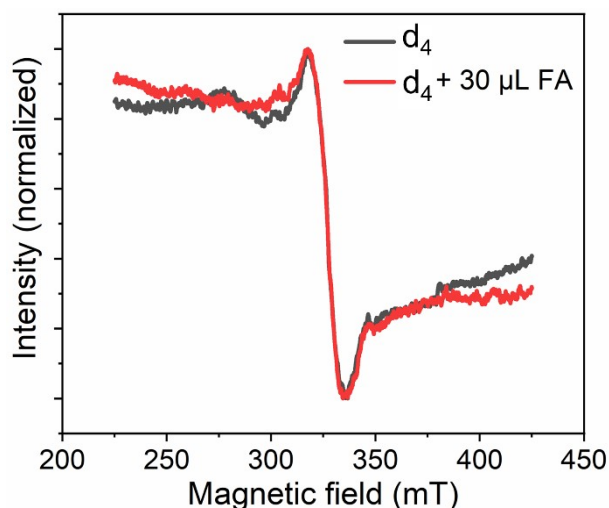


Figure S31. EPR spectra of dispersion d_4 samples with and without FA.

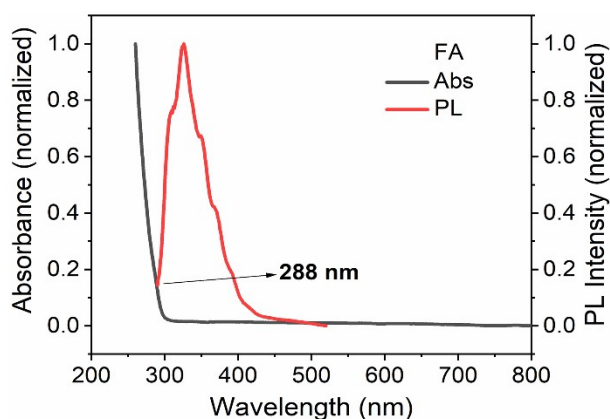


Figure S32. Normalized UV-Vis absorption and PL spectrum of FA solvent.

According to Figure 5e, the oxidation potential of FA (E^{ox}) was determined to be 2.18 V. The potential of Fc/Fc^+ vs vacuum is 4.8 V. The energy level of HOMO of FA can be calculated as: $E_{\text{HOMO}} = -[E^{\text{ox}} - E(\text{Fc}/\text{Fc}^+) + 4.8] \text{ eV} = -[(2.18 - (0.36 + 0.52))/2 + 4.8] \text{ eV} = -6.54 \text{ eV}$. E_g of FA can be determined from the point of intersection between normalized absorption and PL spectrum. E_{LUMO} of FA can be calculated as: $E_{\text{LUMO}} = E_{\text{HOMO}} + E_g = -6.54 + 4.31 = -2.23 \text{ eV}$.

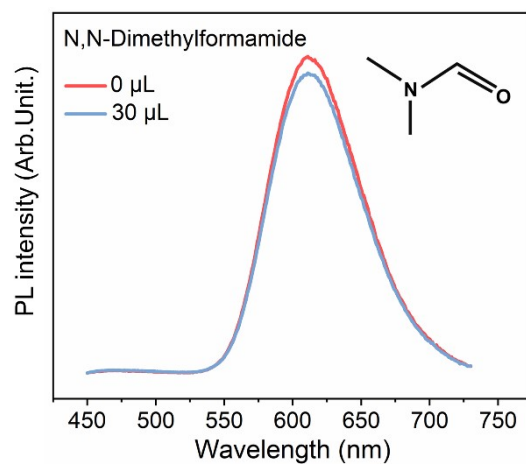


Figure S33. PL spectra of dispersion \mathbf{d}_4 samples (3 mL) with and without 30 μL DMF. No PL brightening was observed after the addition of DMF.

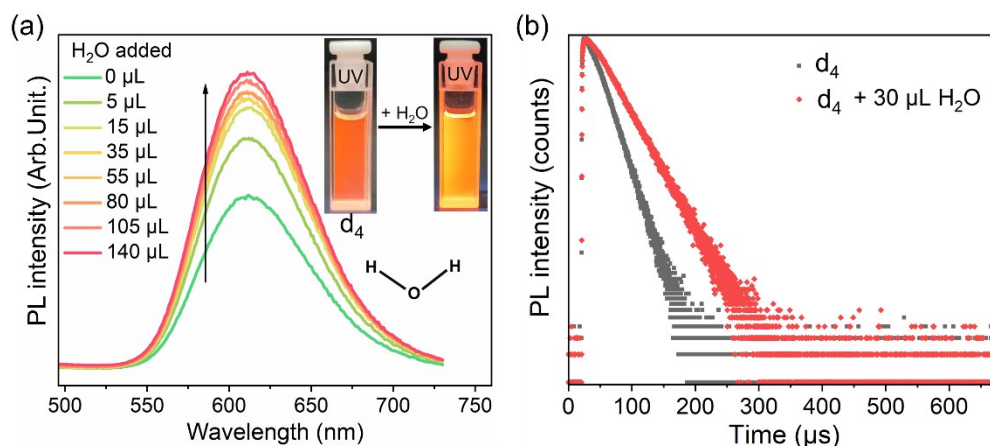


Figure S34. (a) PL spectra of dispersion \mathbf{d}_4 with an increase in amount of dionized H_2O added. Inset: optical images of dispersion \mathbf{d}_4 with and without 30 μL H_2O under UV light irradiation. (b) PL decay curves of dispersion \mathbf{d}_4 with and without 30 μL H_2O . The prolonged decay lifetime of Mn^{2+} emission indicates that energy consumption caused by chloroform molecules was to certain extent blocked owing to the generation of hydrogen bonds.

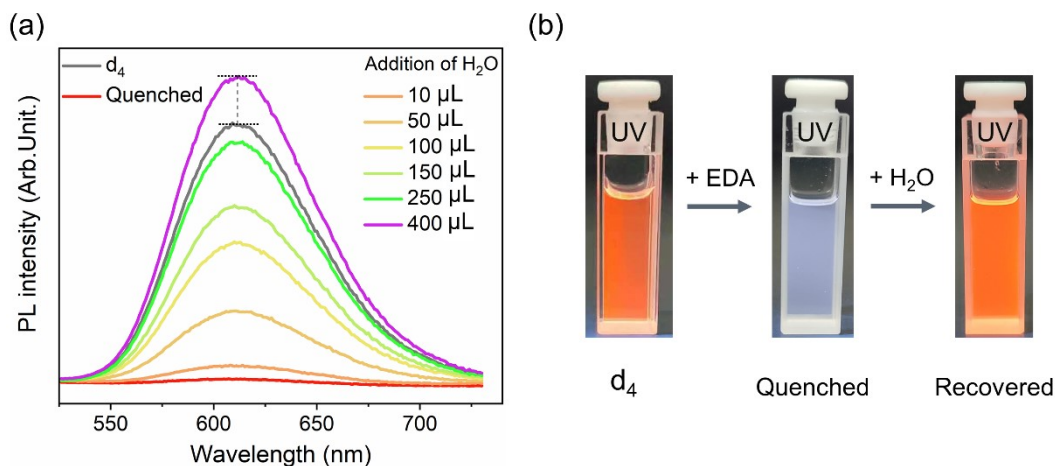


Figure S35. (a) PL spectra of raw d_4 dispersion, EDA-quenched d_4 as well as the emission recovered d_4 treated by the increased addition of H_2O . (b) Optical images of raw d_4 dispersion, EDA-quenched and H_2O -recovered d_4 dispersion under UV light irradiation.

References

- 1 Z. Wu, X. Wang, X. Wang, X. Xu, D. Li, T. Wu, *Chem. Eng. J.*, 2021, **426**, 131216.
- 2 X.-L. Wang, Z. Wu, X. Wang, C. Xue, C. Liu, J. Zhang, R. Zhou, D.-S. Li, T. Wu, *Electrochim. Acta*, 2021, **376**, 138048.
- 3 J. Zhang, X. Chen, W. Li, B. Li, L. Wu, *Langmuir*, 2017, **33**, 12750–12758.
- 4 Q. Zhang, J. Lin, Y.-T. Yang, Z.-Z. Qin, D. Li, S. Wang, Y. Liu, X. Zou, Y.-B. Wu, T. Wu, *J. Mater. Chem. C*, 2016, **4**, 10435–10444.
- 5 Y. Shen, Y. Sun, R. Yan, E. Chen, H. Wang, D. Ye, J. Xu, H. Chen, *Biomaterials*, 2017, **148**, 31–40.
- 6 A. Mallick, A. M. El-Zohry, O. Shekhah, J. Yin, J. Jia, H. Aggarwal, A.-H. Emwas, O. F. Mohammed, M. Eddaoudi, *J. Am. Chem. Soc.*, 2019, **141**, 7245–7249.
- 7 F. Lin, F. Li, Z. Lai, Z. Cai, Y. Wang, O. S. Wolfbeis, X. Chen, X. ACS *Appl. Mater. Interfaces*, 2018, **10**, 23335–23343.
- 8 D. Li, X. Li, T. Zhao, H. Liu, S. Jiang, Q. Zhang, H. Ågren, G. Chen, *ACS Nano*, 2020, **14**, 12596–12604.
- 9 J. Huang, D. Wang, Z. Yue, X. Li, D. Chu, P. Yang, *J. Phys. Chem. C*, 2015, **119**, 27892–27899.
- 10 X. Luo, Y. Han, Z. Chen, Y. Li, G. Liang, X. Liu, T. Ding, C. Nie, M. Wang, F. N. Castellano, K. Wu, *Nat. Commun.*, 2020, **11**, 28.
- 11 S. Sarkar, R. Bose, S. Jana, N. R. Jana, N. Pradhan, *J. Phys. Chem. Lett.*, 2010, **1**, 636–640.
- 12 J. Yu, C. Zhang, *J. Mater. Chem. C*, 2020, **8**, 16463–16469.
- 13 Y. Hou, X. Du, S. Scheiner, D. P. McMeekin, Z. Wang, N. Li, M. S. Killian, H. Chen, M. Richter, I. Levchuk, *Science*, 2017, **358**, 1192–1197.
- 14 Z. Liu, Y. Sun, J. Yuan, H. Wei, X. Huang, L. Han, W. Wang, H. Wang, W. Ma, *Adv. Mater.*, 2013, **25**, 5772–5778.
- 15 K. Zhang, T. Yu, F. Liu, M. Sun, H. Yu, B. Liu, Z. Zhang, H. Jiang, S. Wang, *Anal. Chem.*, 2014, **86**, 11727–33.
- 16 H. Liu, Z. Wu, J. Shao, D. Yao, H. Gao, Y. Liu, W. Yu, H. Zhang, B. Yang, *ACS Nano*, 2017, **11**, 2239–

2247.